

Activation of Sodium Storage Sites in Prussian Blue Analogues via Surface Etching

Wenhao Ren,[†] Mingsheng Qin,[†] Zixuan Zhu,[†] Mengyu Yan,[§] Qi Li,^{*,†} Lei Zhang,[†] Dongna Liu,[†] and Liqiang Mai^{*,†,‡}

[†]State Key Laboratory of Advanced Technology for Materials Synthesis and Processing, Wuhan University of Technology, Wuhan 430070, China

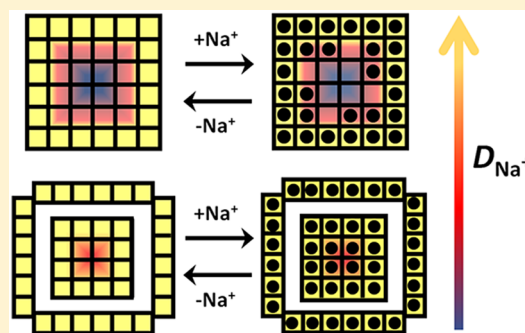
[‡]Department of Chemistry, University of California, Berkeley, California 94720, United States

[§]Materials Science and Engineering Department, University of Washington, Seattle, Washington 98195-2120, United States

S Supporting Information

ABSTRACT: Sodium-ion battery technologies are known to suffer from kinetic problems associated with the solid-state diffusion of Na⁺ in intercalation electrodes, which results in suppressed specific capacity and degraded rate performance. Here, a controllable selective etching approach is developed for the synthesis of Prussian blue analogue (PBA) with enhanced sodium storage activity. On the basis of time-dependent experiments, a defect-induced morphological evolution mechanism from nanocube to nanoflower structure is proposed. Through in situ X-ray diffraction measurement and computational analysis, this unique structure is revealed to provide higher Na⁺ diffusion dynamics and negligible volume change during the sodiation/desodiation processes. As a sodium ion battery cathode, the PBA exhibits a discharge capacity of 90 mA h g⁻¹, which is in good agreement with the complete low spin Fe^{LS}(C) redox reaction. It also demonstrates an outstanding rate capability of 71.0 mA h g⁻¹ at 44.4 C, as well as an unprecedented cycling reversibility over 5000 times.

KEYWORDS: Activation, Prussian blue analogues, etching, sodium ion batteries, solid-state diffusion



To meet the substantially increased energy consumptions, low-cost and long lifespan battery techniques are urgently needed for the electrical grid.^{1–4} Considering the elemental properties as well as abundance, the most promising substitute to the lithium ion battery is the sodium ion battery (SIB).^{5–8} However, SIBs suffer from sluggish dynamics linked to the large ionic radius of Na⁺, leading to the suppressed capacity and limited rate performance.^{9,10} For this reason, Prussian blue analogues (PBAs, A_xM₁[M₂(CN)₆]_y·nH₂O; A: alkaline metal; M: transition metal; 0 ≤ x ≤ 2; y ≤ 1) have attracted growing attentions owing to their intrinsic open framework structure, high theoretical capacity, and large interstitial sites.^{11–13} The room-temperature synthesis procedure and low cost of PBAs are also extremely beneficial toward large-scale applications.^{14,15} However, PBAs suffer from insufficiently utilized low spin (LS) Fe^{LS}(C) redox couples associated with suppressed Na⁺ mobility in bulk structure, resulting in degraded discharge capacity and limited rate capability.¹⁶

Many efforts have been applied to improve the activity of Fe^{LS}(C) sodium storage sites.^{17–19} The Goodenough group²⁰ reported a novel rhombohedral Prussian white (Na_{1.92}Fe[Fe(CN)₆]) with enhanced electrochemical performance as the SIB cathode, but a low capacity contribution of Fe^{LS}(C) reaction was still observed especially under high rate. Jiang et al.¹⁶ created a facile approach to synthesize the ketjen black

decorated PB composite, which exhibited enhanced Na⁺ storage properties for Fe^{LS}(C) sites. Unfortunately, most of the previous efforts failed to take full advantage of the Fe^{LS}(C) redox couple (theoretical capacity: ~90 mA h g⁻¹). New approaches to activate the sodium storage sites associated with Fe^{LS}(C) reaction are urgently needed. To make full use of redox sites, one of the optimal approaches is surface activation since most of the intercalation processes follow the outside-in route.^{21,22} Different from carbon decoration or polymer coating, the surface activation is a process of recrystallization, which not only increases the number of active sites on the surface, but also promotes the activity of reaction site in the central area. Nevertheless, bulk synthesis of PBAs has long been performed via a coprecipitation process, and few researches have led to the surface activation. Therefore, efficient methods for the fabrication of surface activated PBAs are of great significance.

Herein, we report a new surface etching approach to activate the sodium storage sites in the nickel hexacyanoferrate (NiHCF) cathode, which displays a unique nanoflower structure. The formation mechanism of this structure is

Received: April 1, 2017

Revised: June 11, 2017

Published: June 30, 2017

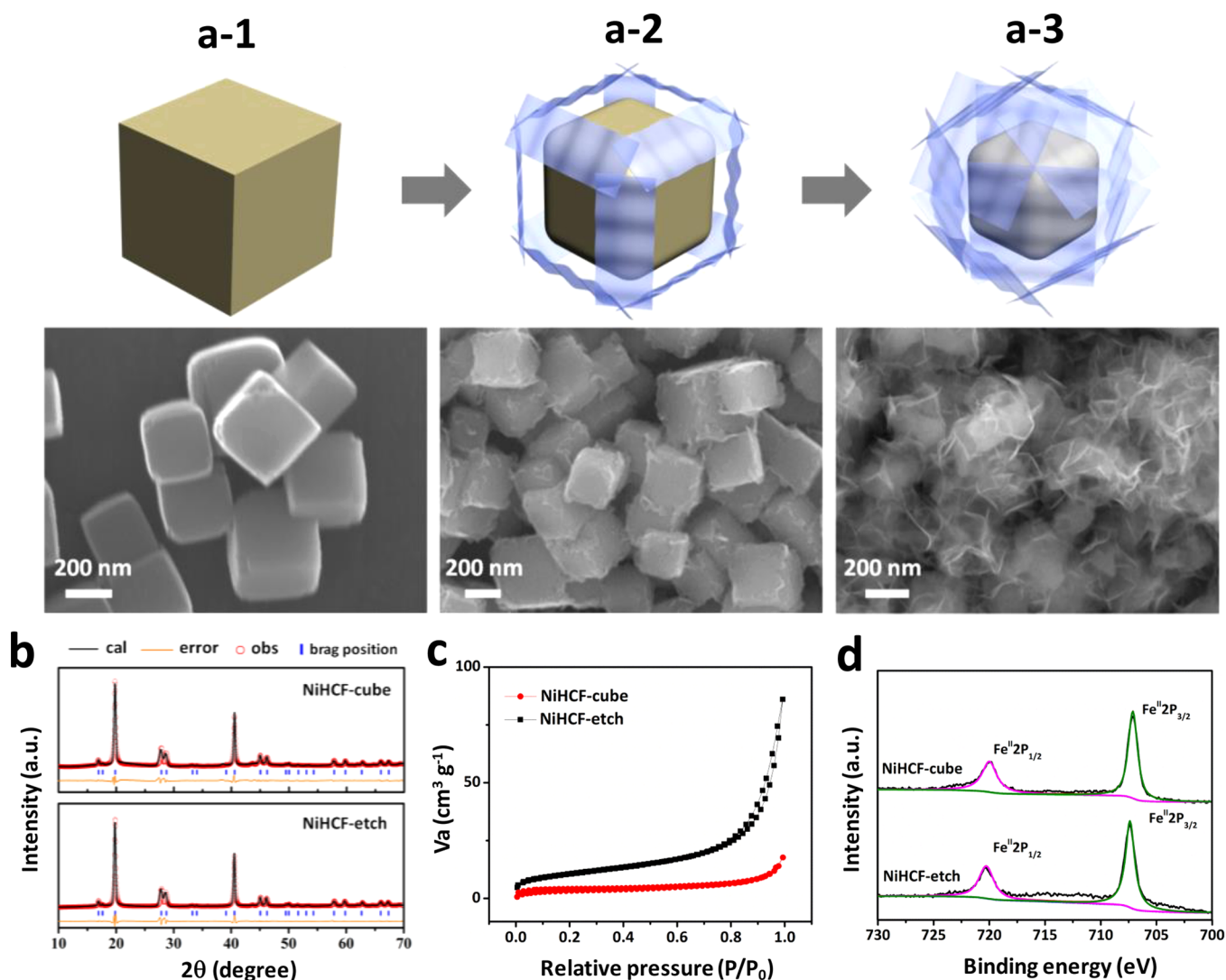


Figure 1. Schematic diagrams accompanied by field-emission scanning electron microscope (FESEM) images of the NiHCF products after the etching time for (a-1) 0 h, (a-2) 0.5 h, (a-3) 6 h. (b) X-ray diffraction (XRD) patterns, (c) Brunauer–Emmett–Teller (BET) surface area and (d) X-ray photoelectron spectroscopy (XPS) of NiHCF-cube and NiHCF-etch.

identified as a defect-induced heterogeneous reaction process. Electrochemical results clearly reveal that the surface activated NiHCF exhibits the complete reaction of Fe^{LS}(C) sites, superior rate capability, and unprecedented cycling stability. The structure–property relationships of NiHCF are well-understood by the outside-in diffusion diagrams combined with the computational analysis, which suggests that the nanoflower structure provides a faster Na⁺ transport kinetics compared with the nanocube among the whole sodiation/desodiation processes.

The etched NiHCF (NiHCF-etch) was prepared by two steps, from the coprecipitation synthesis of NiHCF-cube (NiHCF-cube) to the following alkaline corrosion process. Schematic illustrations accompanied by time-dependent experiments were carried out to clarify the morphological evolution of NiHCF during the etching process (Figure 1a and Figure S1). The pristine NiHCF-cubes are highly uniform with an average size of 300 nm and have sharp edges and corners (Figure 1a-1). After incubating in a sodium hydroxide solution for 0.5 h, the edges of NiHCF-cubes were initially dissolved due to the disassembly of Fe–C≡N–Ni bond, whereas the plane surfaces remain unchanged (Figure 1a-2).²³ It is known that the etching

process of PBAs follows the defect concentration induced inhomogeneous reaction, and these defects can be mainly ascribed to the [Fe(CN)₆]⁴⁻ vacancies. The edges or corners of PBAs are less stable compared with the flat planes, which is consistent with previous reports.²⁴ Then, the etched area extended preferably along each face, and the nanosheet structure emerged on the surface of cubes, which may be attributed to the dissolution–recrystallization processes.^{24,25} Finally, more nanosheets were generated, and the nanoflower structure was formed when the reaction time reached 6 h (Figure 1a-3). Meanwhile, the surface of NiHCF-etch was entirely reassembled, and the size of internal cubes was 100–200 nm. When the etching time was prolonged to 10 h, the inner nanocubes were almost etched away, and the cumulated nanosheet structure was obtained (Figure S2).

From XRD measurement and the inductively coupled plasma (ICP) analysis, the as-synthesized NiHCF-cube and NiHCF-etch are taken to be rhombohedral Na_{0.96}NiHCF·1.02H₂O and Na_{1.11}NiHCF·0.71H₂O (Figure 1b and Table S1). The increase of Na contents in NiHCF-etch is attributed to the concentration diffusion of Na⁺ from sodium citrate/sodium hydroxide solution into the structure accompanied by the

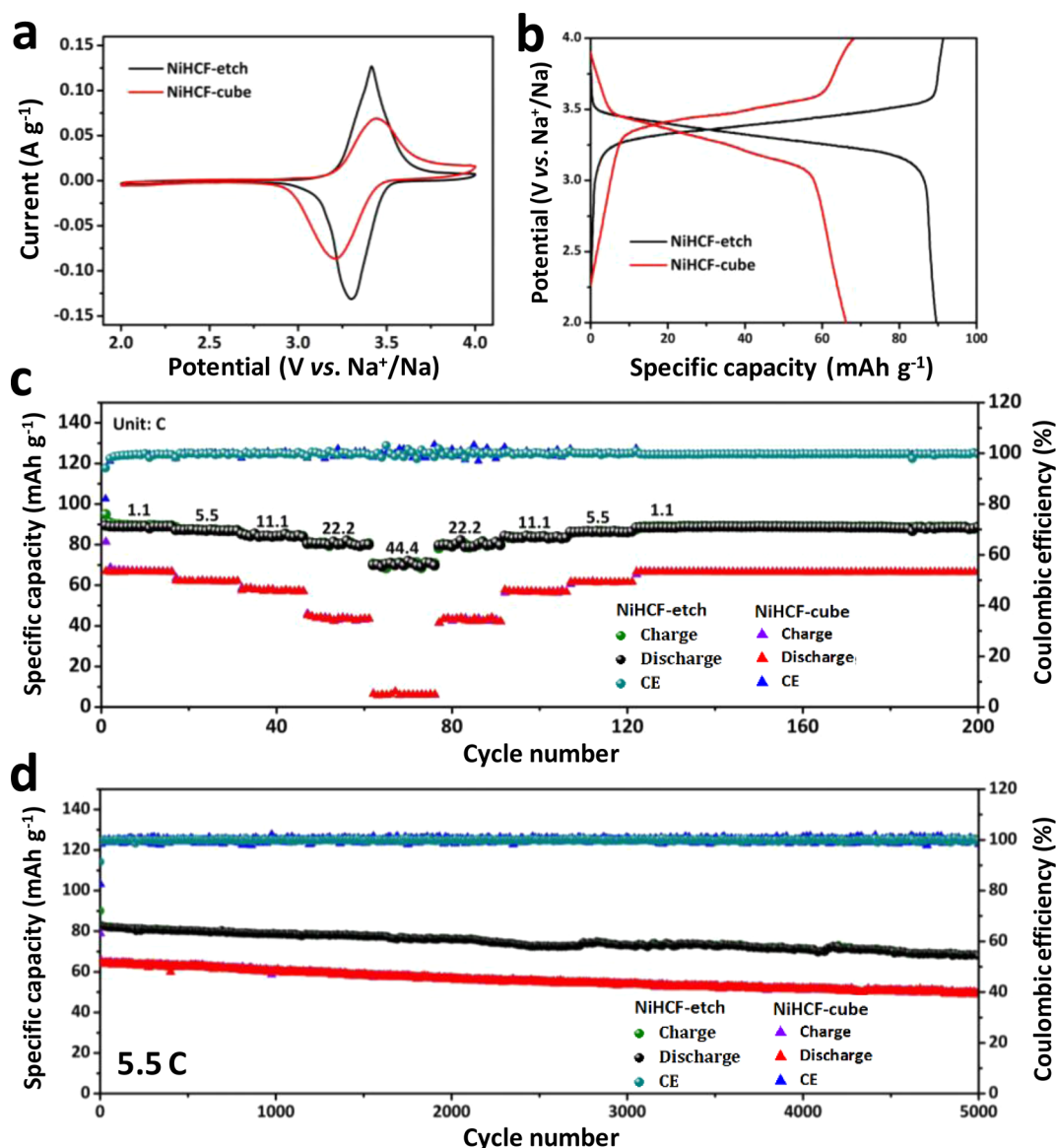


Figure 2. (a) CV profiles and (b) charge–discharge curves of NiHCF-cube and NiHCF-etch at the second cycle. (c) Rate performance and (d) cycling stability of NiHCF-cube and NiHCF-etch.

etching process. The atomic ratio of Fe/Ni in NiHCF-cube and NiHCF-etch are 0.92 and 0.80, respectively, indicating the decomposition of Fe–C≡N–Ni bond and loss of Fe²⁺ during etching, which is consistent with previous report.²³ Besides, the refined XRD results by Rietveld method (Topas software) indicate that the lattice parameter a increased from 6.338 Å for NiHCF-etch to 6.344 Å for the NiHCF-cube sample. The crystal structure of NiHCF is shown in Figure S3, where high-spin (HS) Ni ions are coordinated to nitrogen atoms and low-spin (LS) Fe ions are coordinated to carbon atoms, forming a three-dimensional network with Ni^{II}–N≡C–Fe^{II} chains.^{26,27} The BET surface area also increased from 12.7 to 38.0 m² g⁻¹ after the formation of nanoflower structure (Figure 1c). A small content of water is assessed for NiHCF-etch (0.71 H₂O/f.u.) compared with NiHCF-cube (1.02 H₂O/f.u.) based on the weight loss in the TGA curve (50 < T < 200 °C, Figure S4). Then, the XPS, Raman, and Fourier transform infrared spectra (FTIR) were carried out to identify the valence state and chemical bonding interaction of NiHCF (Figure 1d, Figures S5 and S6) before and after etching. All of the results show that

the valence state of Fe and Ni are +2, and no bonding variation except the slight hydroxylation of the surface is observed.^{28–30}

To investigate the electrochemical performance of electrodes, sodium half cells were fabricated. The redox properties of the two samples were explored by cyclic voltammetry (CV) (Figure 2a) at a scan rate of 0.1 mV s⁻¹. A pair of well-defined redox peaks at ~3.4 V appear in NiHCF-etch, corresponding to the equilibrium voltage of Fe^{II}/Fe^{III}.³¹ Moreover, NiHCF-etch has a larger curve area and higher redox peak current compared with NiHCF-cube, indicating that the NiHCF-etch possesses higher specific capacity as well as faster kinetics for Na⁺ insertion/extraction.³² The initial galvanostatic charge–discharge curves of the samples at 1.1 C (1 C = 90 mA g⁻¹) are presented (Figure S7). It is known that the Coulombic efficiencies of PBAs at the first cycle are generally below the 100%, which is attributed to the interstitial water.³³ Therefore, the enhanced Coulombic efficiency of NiHCF-etch compared with NiHCF-cube may be assigned to the smaller content of interstitial water as confirmed by TGA (Figure S4). Notably, the specific capacity of NiHCF-etch (~90 mA h g⁻¹) at the second cycle

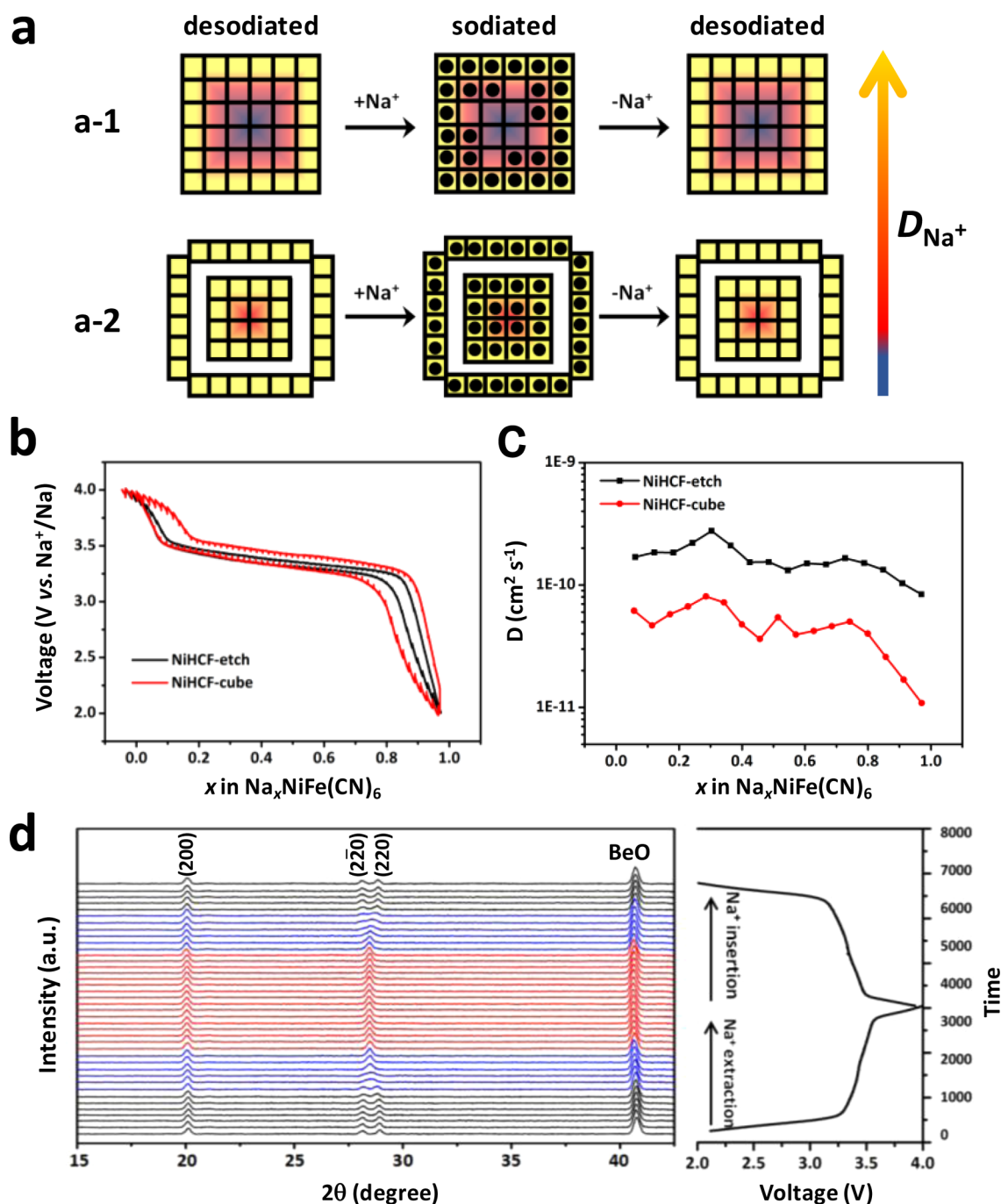


Figure 3. (a) Outside-in diffusion route of Na^+ in NiHCF-cube and NiHCF-etch. (b) The GITT curves of NiHCF-cube and NiHCF-etch after normalization. (c) The calculated diffusion coefficients versus state of discharge. (d) In situ XRD pattern of NiHCF-etch.

(Figure 2b) can be well-identified as the complete reaction of $\text{Fe}^{\text{LS}}(\text{C})$ redox couples, which corresponds to the insertion/extraction of almost 1.0 Na/f.u., considerably exceeding the previous results (Table S2). By contrast, the specific capacity of the NiHCF-cube is only 66 mA h g^{-1} (0.73 Na/f.u.) with a higher overpotential. In addition, the rate capabilities of NiHCF-etch and NiHCF-cube were also evaluated ranging from 1.1 C to an ultrahigh rate of 44.4 C (Figure 2c). The NiHCF-etch exhibits a substantial capacity of 70.9 mA h g^{-1} even at the ultrahigh rate of 44.4 C (60 s for a charge or a discharge process), corresponding to 78.8% retention of the capacity at 1.1 C, whereas the discharge capacities of NiHCF-cube are only 66.8 mA h g^{-1} at 1.1 C and 5.9 mA h g^{-1} at 44.4

C. The long-term structural durability of the electrodes at 5.5 C was also investigated (Figure 2d). Notably, the capacity retentions of NiHCF-etch and NiHCF-cube reach up to 83.2% and 76.9% after 5000 cycles, and the Coulombic efficiency remains $\sim 100\%$ in the overall battery operation, suggesting excellent reversibility. This is the longest cycle life of PBAs in SIBs ever reported, and such enhanced performance demonstrates the success of surface activation strategy.

The solid-state diffusion process of Na^+ in electrodes follows the outside-in route (Figure 3a), and their mobility becomes the limiting factor for an electrode reaction.³⁴ To utilize all of the reaction sites in the NiHCF-cube (Figure 3a-1), Na^+ ions are required to pass through a long distance from surface into

center, leading to the suppressed reactivity in the central part. Meanwhile, for the NiHCF-etch, Na^+ ions merely need to diffuse through a much shorter distance so as to occupy all of the insertion sites (Figure 3a–2), and a large proportion of the reaction sites in central area may be accessed. Furthermore, a galvanostatic intermittent titration technique (GITT) was employed to analyze the solid-state diffusion kinetics of Na^+ (Figure 3b). The electrodes were first cycled at 1.1 C for three times to reach the normal operation state prior to GITT test. The chemical diffusion coefficient of Na^+ (D_{Na}) as a function of stoichiometry (x) after normalization were computationally analyzed according to the GITT (Figure 3c and Figure S8).³⁵ The calculated $D_{\text{Na}}^{\text{GITT}}$ for the NiHCF-cube and NiHCF-etch is between 10^{-10} – 10^{-11} $\text{cm}^2 \text{s}^{-1}$ and 10^{-9} – 10^{-10} $\text{cm}^2 \text{s}^{-1}$, respectively. A similar trend is observed for both electrodes with a minimum D_{Na} at $x \approx 1$ (sodiated state), at which the $D_{\text{Na}}^{\text{GITT}}$ of the NiHCF-cube drops rapidly to about 10^{-11} $\text{cm}^2 \text{s}^{-1}$, indicating a sluggish electrochemical kinetics along with insertion of Na^+ . By contrast, the $D_{\text{Na}}^{\text{GITT}}$ of the NiHCF-etch does not decline significantly after the sodiation process, which is in good agreement with the outside-in diffusion mechanism presented in Figure 3a. CV^{36,37} (Figure S9) and electrochemical impedance spectroscopy³⁸ (EIS, Figure S10) tests were also conducted to calculate D_{Na} , and the results are consistent with GITT analysis. To further verify the above calculations, the GITT and EIS analyses based on lithium batteries were also carried out (Figure S11). Similar to the sodiated/desodiated processes, the diffusivity of NiHCF-etch versus Li^+/Li is also higher than NiHCF-cube at each state ($0 \leq x \leq 1$), indicating the faster solid-state diffusion of alkali cations in the NiHCF-etch.

The electrochemical reaction mechanism of NiHCF-etch was investigated through in situ XRD tests with Co $K\alpha$ X-ray source (Figure 3d). The employ of Co $K\alpha$ X-ray source can effectively avoid the signal interference by Fe or Ni. Remarkably, the peak shift in XRD patterns is negligible during the Na^+ extraction process, which means the lattice parameters of the NiHCF-etch remain almost unchanged. This redox reaction is advantageous because the crystal structure of NiHCF-etch is avoided from large volume variation and stress–strain during the Na^+ insertion/extraction, and thus prevents the collapse of the crystal framework. With the decrease of Na contents, the crystal structure of the NiHCF-etch gradually evolves from rhombohedral to cubic, demonstrating that the low Na concentration improves the crystal symmetry.³⁹ Conversely, the structure change is highly reversible, and peaks return to the original positions after the complete insertion of Na^+ . The ex situ XRD analysis was also performed on NiHCF-cube, and all of the peaks exhibit the same trend with the in situ XRD results (Figure S12). The overall electrochemical reaction is based on LS-Fe^{2+} ($t_{2g}^6 e_g^0$) \sim LS-Fe^{3+} ($t_{2g}^5 e_g^0$) and can be described by following expression: rhombohedral $\text{Na}_x\text{Ni}^{\text{II}}\text{Fe}^{\text{II}}(\text{CN})_6 \leftrightarrow$ cubic $\text{Na}_{x-1}\text{Ni}^{\text{II}}\text{Fe}^{\text{III}}(\text{CN})_6$ (Figure S13).

In summary, a surface-activated NiHCF-etch cathode with fast Na^+ diffusion kinetics is obtained through a preferential etching strategy. Based on time-dependent experiments, a defect-induced morphological evolution mechanism from nanocube to nanoflower is proposed. Compared with previous reports, the NiHCF-etch overcomes the problem of underutilized $\text{Fe}^{\text{LS}}(\text{C})$ redox sites. It exhibits a specific capacity of 90 mA h g^{-1} , an extremely high rate capability of 71.0 mA h g^{-1} at 44.4 C, and the unprecedented cycle life over 5000 times, enabling the NiHCF-etch a promising cathode for a long

lifespan and high-power SIBs. Besides, the structure–property relationships of the NiHCF-etch have been well-understood via the diffusion diagrams combined with the computational analysis, which indicates that the surface activation is able to greatly improve the Na^+ diffusion dynamics. It is expected that this new surface activation strategy can also be applied to construct other materials with a faster ionic mobility.

■ ASSOCIATED CONTENT

Supporting Information

The Supporting Information is available free of charge on the ACS Publications website at DOI: 10.1021/acs.nanolett.7b01366.

Experimental section and additional figures (PDF)

■ AUTHOR INFORMATION

Corresponding Authors

*E-mail: mlq518@whut.edu.cn.

*E-mail: qi.li@whut.edu.cn.

ORCID

Liqiang Mai: 0000-0003-4259-7725

Author Contributions

W.H.R. and M.S.Q. contributed equally to this work. L.Q.M., W.H.R., and Q.L. designed the experiments. W.H.R., M.S.Q., Z.X.Z., and D.N.L. performed the experiments. W.H.R., M.S.Q., Z.X.Z., M.Y.Y., and L.Z. discussed the interpretation of results and cowrote the paper. All authors discussed the results and commented on the manuscript.

Notes

The authors declare no competing financial interest.

■ ACKNOWLEDGMENTS

This work was supported by the National Key Research and Development Program of China (2016YFA0202603), the National Basic Research Program of China (2013CB934103), the Programme of Introducing Talents of Discipline to Universities (B17034), the National Natural Science Foundation of China (51521001), the National Natural Science Fund for Distinguished Young Scholars (51425204), the Fundamental Research Funds for the Central Universities (WUT: 2016III001, 2017IVA100), and the project of Innovative Group for Low Cost and Long Cycle Life Na-ion Batteries R&D and industrialization of Guangdong Province (2014ZT05N013). Prof. Liqiang Mai gratefully acknowledges financial support from China Scholarship Council (no. 201606955096).

■ REFERENCES

- (1) Larcher, D.; Tarascon, J. M. *Nat. Chem.* **2015**, *7*, 19–29.
- (2) Wang, R. Y.; Wessells, C. D.; Huggins, R. A.; Cui, Y. *Nano Lett.* **2013**, *13*, 5748–5752.
- (3) Ren, W.; Zhu, Z.; An, Q.; Mai, L. *Small* **2017**, *13*, 1604181–1604193.
- (4) Yao, B.; Huang, L.; Zhang, J.; Gao, X.; Wu, J.; Cheng, Y.; Xiao, X.; Wang, B.; Li, Y.; Zhou, J. *Adv. Mater.* **2016**, *28*, 6353–6358.
- (5) Liu, Y.; Wang, H.; Lin, D.; Zhao, J.; Liu, C.; Xie, J.; Cui, Y. *Nano Res.* **2017**, *10*, 1213–1222.
- (6) Yabuuchi, N.; Kubota, K.; Dahbi, M.; Komaba, S. *Chem. Rev.* **2014**, *114*, 11636–11682.
- (7) Goodenough, J. B.; Park, K. S. *J. Am. Chem. Soc.* **2013**, *135*, 1167–1176.

- (8) Xu, X.; Cao, R.; Jeong, S.; Cho, J. *Nano Lett.* **2012**, *12*, 4988–4991.
- (9) Xiang, X.; Zhang, K.; Chen, J. *Adv. Mater.* **2015**, *27*, 5343–5364.
- (10) Johansson, A.; Widenkvist, E.; Lu, J.; Boman, M.; Jansson, U. *Nano Lett.* **2005**, *5*, 1603–1606.
- (11) Li, W. J.; Chou, S. L.; Wang, J. Z.; Wang, J. L.; Gu, Q. F.; Liu, H. K.; Dou, S. X. *Nano Energy* **2015**, *13*, 200–207.
- (12) Hu, M.; Belik, A. A.; Imura, M.; Yamauchi, Y. *J. Am. Chem. Soc.* **2013**, *135*, 384–391.
- (13) Wang, H.; Wang, L.; Chen, S.; Li, G.; Quan, J.; Xu, E.; Song, L.; Jiang, Y. *J. Mater. Chem. A* **2017**, *5*, 3569–3577.
- (14) Hu, M.; Furukawa, S.; Ohtani, R.; Sukegawa, H.; Nemoto, Y.; Reboul, J.; Kitagawa, S.; Yamauchi, Y. *Angew. Chem., Int. Ed.* **2012**, *51*, 984–988.
- (15) Liu, Y.; Qiao, Y.; Zhang, W.; Li, Z.; Ji, X.; Miao, L.; Yuan, L.; Hu, X.; Huang, Y. *Nano Energy* **2015**, *12*, 386–393.
- (16) Jiang, Y.; Yu, S.; Wang, B.; Li, Y.; Sun, W.; Lu, Y.; Yan, M.; Song, B.; Dou, S. *Adv. Funct. Mater.* **2016**, *26*, 5315–5321.
- (17) You, Y.; Yao, H. R.; Xin, S.; Yin, Y. X.; Zuo, T. T.; Yang, C. P.; Guo, Y. G.; Cui, Y.; Wan, L. J.; Goodenough, J. B. *Adv. Mater.* **2016**, *28*, 7243–7248.
- (18) Song, J.; Wang, L.; Lu, Y.; Liu, J.; Guo, B.; Xiao, P.; Lee, J. J.; Yang, X. Q.; Henkelman, G.; Goodenough, J. B. *J. Am. Chem. Soc.* **2015**, *137*, 2658–2664.
- (19) You, Y.; Wu, X. L.; Yin, Y. X.; Guo, Y. G. *Energy Environ. Sci.* **2014**, *7*, 1643–1647.
- (20) Wang, L.; Song, J.; Qiao, R.; Wray, L. A.; Hossain, M. A.; Chuang, Y. D.; Yang, W.; Lu, Y.; Evans, D.; Lee, J. J.; Vail, S.; Zhao, X.; Nishijima, M.; Kakimoto, S.; Goodenough, J. B. *J. Am. Chem. Soc.* **2015**, *137*, 2548–2554.
- (21) Lin, F.; Markus, I. M.; Nordlund, D.; Weng, T. C.; Asta, M. D.; Xin, H. L.; Doeff, M. M. *Nat. Commun.* **2014**, *5*, 3529–3527.
- (22) Ding, J.; Wang, H.; Li, Z.; Cui, K.; Karpuzov, D.; Tan, X.; Kohandehghan, A.; Mitlin, D. *Energy Environ. Sci.* **2015**, *8*, 941–955.
- (23) Zhang, W.; Zhao, Y.; Malgras, V.; Ji, Q.; Jiang, D.; Qi, R.; Ariga, K.; Yamauchi, Y.; Liu, J.; Jiang, J. S.; Hu, M. *Angew. Chem., Int. Ed.* **2016**, *55*, 8228–8234.
- (24) Han, L.; Yu, X. Y.; Lou, X. W. *Adv. Mater.* **2016**, *28*, 4601–4605.
- (25) Ren, W.; Zheng, Z.; Xu, C.; Niu, C.; Wei, Q.; An, Q.; Zhao, K.; Yan, M.; Qin, M.; Mai, L. *Nano Energy* **2016**, *25*, 145–153.
- (26) Ling, C.; Chen, J.; Mizuno, F. *J. Phys. Chem. C* **2013**, *117*, 21158–21165.
- (27) Li, W. J.; Chou, S. L.; Wang, J. Z.; Kang, Y. M.; Wang, J. L.; Liu, Y.; Gu, Q. F.; Liu, H. K.; Dou, S. X. *Chem. Mater.* **2015**, *27*, 1997–2003.
- (28) Kulesza, P. J.; Malik, M. A.; Denca, A.; Strojek, J. *Anal. Chem.* **1996**, *68*, 2442–2446.
- (29) Yang, D.; Liao, X. Z.; Huang, B.; Shen, J.; He, Y. S.; Ma, Z. F. *J. Mater. Chem. A* **2013**, *1*, 13417–13421.
- (30) Jeerage, K. M.; Steen, W. A.; Schwartz, D. T. *Langmuir* **2002**, *18*, 3620–3625.
- (31) Wessells, C. D.; Peddada, S. V.; Huggins, R. A.; Cui, Y. *Nano Lett.* **2011**, *11*, 5421–5425.
- (32) Ren, W.; Yao, X.; Niu, C.; Zheng, Z.; Zhao, K.; An, Q.; Wei, Q.; Yan, M.; Zhang, L.; Mai, L. *Nano Energy* **2016**, *28*, 216–223.
- (33) Lu, Y.; Wang, L.; Cheng, J.; Goodenough, J. B. *Chem. Commun.* **2012**, *48*, 6544–6546.
- (34) Taberna, P. L.; Mitra, S.; Poizot, P.; Simon, P.; Tarascon, J. M. *Nat. Mater.* **2006**, *5*, 567–573.
- (35) An, Q.; Li, Y.; Yoo, H. D.; Chen, S.; Ru, Q.; Mai, L.; Yao, Y. *Nano Energy* **2015**, *18*, 265–272.
- (36) Brezesinski, T.; Wang, J.; Tolbert, S. H.; Dunn, B. *Nat. Mater.* **2010**, *9*, 146–151.
- (37) Augustyn, V.; Come, J.; Lowe, M. A.; Kim, J. W.; Taberna, P. L.; Tolbert, S. H.; Abruña, H. D.; Simon, P.; Dunn, B. *Nat. Mater.* **2013**, *12*, 518–522.
- (38) Wang, H.; Huang, K.; Ren, Y.; Huang, X.; Liu, S.; Wang, W. *J. Power Sources* **2011**, *196*, 9786–9791.
- (39) Matsuda, T.; Kim, J.; Moritomo, Y. *J. Am. Chem. Soc.* **2010**, *132*, 12206–12207.